Journal of the European Ceramic Society 42 (2022) 1576–1584

Contents lists available at ScienceDirect

Journal of the European Ceramic Society

journal homepage: www.elsevier.com/locate/jeurceramsoc

Evolution of the structure and chemical composition of the interface between multi-component silicate glasses and yttria-stabilized zirconia after 40,000 h exposure in air at 800 °C

Qianying Guo [a], Tianli Feng [b,c], Michael J. Lance [d], Kinga A. Unocic [a,*], Sokrates T. Pantelides [a,c], Edgar Lara-Curzio [d,*]

[a] Center for Nanophase Materials Sciences, Oak Ridge National Laboratory, Oak Ridge, TN 37831, USA
[b] Buildings and Transportation Science Division, Oak Ridge National Laboratory, Oak Ridge, TN 37831, USA
[c] Department of Physics and Astronomy and Department of Electrical Engineering and Computer Science, Vanderbilt University, Nashville, TN 37235, USA
[d] Materials Science and Technology Division, Oak Ridge National Laboratory, Oak Ridge, TN 37831, USA

ARTICLE INFO

Keywords:
Multicomponent silicate glass
Glass seals
Yttria-stabilized zirconia
Solid-oxide fuel cells
Phase transformation

ABSTRACT

The chemical and structural stability of two commercial multicomponent silicate glasses (SCN and G6) in contact with yttria-stabilized zirconia (YSZ) was investigated after exposure times of up to 40,000 h in air at 800 °C. With exposure time, interfacial layers develop at the SCN-YSZ and G6-YSZ interfaces, which were characterized in detail using both quantitative chemical analysis and atomic-resolution imaging. At the SCN-YSZ interface, a Ca-Ba-Si-O reaction phase was found to grow by diffusion control. In G6-YSZ, Raman spectroscopy and electron microscopy revealed a disorganized interfacial reaction later between G6 and YSZ, and the occurrence of cubic to tetragonal to monoclinic phase transformations in YSZ. This microstructural evolution is discussed in terms of devitrification resistance of glass and diffusion processes at interfaces.

1. Introduction

Solid-oxide fuel cells (SOFCs) are electrochemical devices that convert the chemical energy stored in fuels to electrical energy [1]. These devices are attractive because of their high conversion efficiency and production of electricity from a wide variety of fuels [1]. Most SOFC configurations require seals to prevent the intermixing of fuel and air, and the selection of sealing materials must meet several demanding requirements. For example, the materials must exhibit chemical and thermal expansion compatibility with other cell components—including electrodes, electrolyte, and current collectors—over the entire range of operating temperatures and the system lifetime, which is measured in tens of thousands of hours. Seals must also be chemically stable in both air and SOFC fuel environments, electrically insulating, easy to manufacture a cost-effective [1].

Among the various SOFC sealing strategies, compliant glass seals are attractive because their physical and mechanical properties, including their rheological behavior, can be tuned by changing their chemical composition to facilitate their manufacture, to exhibit compliance, and to promote self-healing behavior [2–4]. Critical to the successful implementation of compliant glass sealing concepts for SOFCs is the long-term structural stability of the glass, particularly its resistance to crystallization—which translates into its ability to flow and heal cracks—which are some of its most attractive features [5]. Compliant glasses are also key components of engineered glass sealing concepts, which are based on the addition of crystalline phases to control viscosity, to enable tuning of physical properties, such as viscosity, and to address large temperature gradients, not only on cell planes for planar fuel cells, but also along the height of the stack [4,6–8].

Previous studies of the durability of compliant glass seals for SOFCs have been limited to relatively short periods of time [2,5,6,9–13]. One exception is a study of the evolution of the microstructure of the two commercially available glasses investigated in this paper (SCN and G6) after 10,000 h of exposure in air and gas mixtures of H_2+N_2+H_2O at 800 °C when in contact with YSZ or Al_2O_3 substrates [14]. That study revealed that while several crystalline phases precipitated from the glasses, overall they had sufficient resistance to devitrification, which is required to exhibit crack healing behavior.

In this paper, we report results from the microstructural characterization of the interfacial region between SCN and G6 glasses and an YSZ

* Corresponding authors.
E-mail addresses: unocicka@ornl.gov (K.A. Unocic), laracurzioe@ornl.gov (E. Lara-Curzio).

https://doi.org/10.1016/j.jeurceramsoc.2021.11.013
Received 2 May 2021; Received in revised form 1 November 2021; Accepted 8 November 2021
Available online 9 November 2021

substrate after up to 40,000 h exposure in air at 800 °C in order to assess the long-term interfacial stability of these glasses when in contact with YSZ for SOFC applications. This type of studies are necessary considering that the expected service life of SOFCs is between 10 and 15 years and our current inability to predict the kinetics of crystal nucleation and growth for multicomponent glasses, such as SCN and G6, from first principles.

2. Experimental and computational modeling procedures

Two commercial multicomponent silicate glasses, SCN glass (SEM-COM Co. Inc., Toledo, OH 43623, USA), and G6 glass (Whatman Ltd., Piscataway, NJ 08855, USA), were used in this investigation. Some of the main compositional differences between SCN and G6 glass include the concentrations of boron, potassium and zinc. For example, G6 glass contains higher concentrations of boron (15.4 vs. 0.3 at.%) and zinc (2.5 vs. 0.0 at%), where boron is added to control the thermal properties of the glass and the adhesion/wetting behavior of the glass on the substrate [5,14]. The compositions of these two glasses, as determined by inductively coupled plasma–acoustic emission spectroscopy (ICP-AES), are listed in Table 1 [14,15].

The test specimen preparation procedure is illustrated in Fig. 1. Either a compressed SCN pellet or a stack of G6 disks was placed onto dense 8 mol % YSZ substrates (Fuel Cell Materials, Lewis Center, OH 43035, USA). Then the glass–substrate combinations were sintered for 2 h at 850 °C to promote a continuous bond between them (Fig. 1b). A more detailed discussion of test sample preparation can be found elsewhere [14,15]. Afterward, the specimens were subjected to environmental exposures in air inside a box furnace maintained at 800 °C. Test specimens were retrieved after 100, 10,000, 25,000 and 40,000 h and subsequently sectioned in half. One half was polished and for this study, characterized at the interface between the glass and substrate by field emission scanning electron microscopy (FE-SEM) using a JEOL 6500 F (Fig. 1c). TEM thin samples for STEM analysis were prepared by the *in situ* lift-out technique [16,17] using a focused ion beam (FIB)-SEM (Hitachi model NB5000), as illustrated in Fig. 1c. The final thinning step was performed at 5 kV, followed by nanomilling at 900 eV for 10 min (Fishione Nanomill model 1040) to remove surface ion beam damage from sample preparation. The morphology and elemental distribution at the glass/YSZ substrate interfaces were studied by STEM-EDS analysis using an FEI F200X Talos S/TEM operated at 200 kV and equipped with a Super-X EDS system with four silicon-drift detectors (Bruker XFlash 120 mm^2). HR-STEM imaging was performed on an aberration-corrected Nion UltraSTEM 100 operated at 100 kV to reveal the atomic structure and to identify the nanosize phases at the glass/YSZ substrate interface. To prevent and/or decrease any potential electron beam damage during imaging and spectroscopic analysis, the current of the electron beam was maintained at 250 pA for collecting EDS elemental maps and at ~40 pA for acquiring atomic-resolution images. EDS quantitative elemental maps for chemical information at interfaces were acquired using the standardless Cliff–Lorimer method in Bruker Quantax Esprit software.

Raman spectra were collected via Raman microprobe with a Nd:YAG laser operating at 532 nm. A 100× magnification objective lens was used, resulting in a spot size of ~1 μm. Maps were collected at the glass/YSZ interface with 0.2 μm steps between acquisition points. Typical maps were composed of >20,000 Raman spectra. YSZ phases were determined using principal component analysis routines available with the vendor software (WiRE 5.2).

Table 1
Chemical composition of SCN and G6 glasses based on inductively coupled plasma atomic emission spectroscopy.

Element	SCN (at.%)	G6 (at.%)
Si	63.5	52.7
K	11.1	2.3
Ba	3.1	1.5
Na	11.7	15.2
Ca	4.1	3.5
Al	4.1	5.2
Mg	1.7	1.8
Ti	0.4	0
B	0.3	15.4
Zn	0	2.5
Fe	0	0.1

3. Results

The cross-sections of SCN-YSZ specimens exposed for different periods of time in air at 800 °C are shown in Fig. 2, revealing the general morphology and chemical composition of the interfaces. The dark spots in the YSZ substrate are pores. Fig. 2a shows the cross-section of the SCN-YSZ exposed in air at 800 °C for 100 h (SCN-YSZ-100 sample). The interface between SCN and YSZ was sharp without any additional contrast either at the interface or in the glass. After 10,000 h, a thin reaction layer was observed at the SCN/YSZ interface, along with some small crystals in the glass phase near the interface (Fig. 2b). After 25,000 h, the microstructure of the SCN/YSZ interface (Fig. 2c) was similar to that after 10,000 h, but measurements revealed that the thickness of the reaction layer had increased from ~120 nm to ~150 nm. Finally, after 40,000 h of exposure in air, both the thickness of the reaction layer and the density of the crystalline contrasts in the glass increased compared with shorter exposure times. Importantly, no chemical or structural changes were observed in the YSZ substrate after 40,000 h, even at the interface with the thin reaction layer generated during exposure, as is discussed in the STEM analysis of this paper.

A similar SEM analysis was performed on the G6-YSZ system (Fig. 3). The cross-section analysis at the interfacial region after exposure to air for 100 h at 800 °C (Fig. 3a) reveals the presence of a reaction layer with a thickness of 0.49 ± 0.08 μm between G6 and YSZ. After 10,000 h, the reaction layer became thicker (2.29 ± 0.33 μm) and it consisted of plate-shaped structures, with glass filling the spaces between the plates. After 25,000 h, the reaction layer grew even thicker (3.2 ± 0.4 μm) and segregation was observed in the glass phase (Fig. 3c). Subsequently, based on the SEM-EDS maps, these phases were rich in barium (Ba) and silicon (Si) (Fig. S1). Several spherical dark shapes were observed at the edge of the reaction layer in contact with the YSZ substrate. Furthermore, continuous horizontal cracks in the Ba-Si segregation region in the glass were observed [14,15,18]. Microstructural characterization of the 40,000 h G6-YSZ sample also revealed a reaction layer rich in Ba-Si, cracks above and spherical voids at the bottom of the Ba-Si rich segregation region. The only difference between the interfaces after 25,000 and 40,000 h was the thickness of the reaction layer, which extended from 3.2 ± 0.4 μm to 3.61 ± 0.35 μm, respectively.

The thickness measurements of the reaction layer formed in SCN-YSZ and G6-YSZ, versus the square root of exposure time in air at 800 °C, are presented in Fig. 4, which shows that the thickness of the reaction layer increased linearly with the square root of exposure time. The SEM images of the cross-sections (Figs. 2 and 3) highlight the main differences between the two. For example, the thickness of the reaction layer in the SCN-YSZ sample (<0.20 μm) is much smaller than that of the G6-YSZ sample (0.5 μm vs. 3.5 μm). After 100 h exposure, no reaction layer was observed in SCN-YSZ, whereas a ~ 0.5 μm thick reaction layer was observed in the G6-YSZ system. In Fig. 4, the plot of interphase thickness vs. exposure time includes dashed lines corresponding to linear regression analysis of the data. These results suggest that the thickness of the reaction layer was controlled by diffusion of ions, as discussed in the following sections [19]. The regression line for the SCN-YSZ data set extrapolates to the coordinates (0,0), suggesting the absence of an incubation period. However, the regression line for the G6-YSZ data set extrapolates to a finite value of the reaction layer thickness, suggesting a different mechanism at the onset of its formation, which is consistent with its complex, multilayered structure [14].

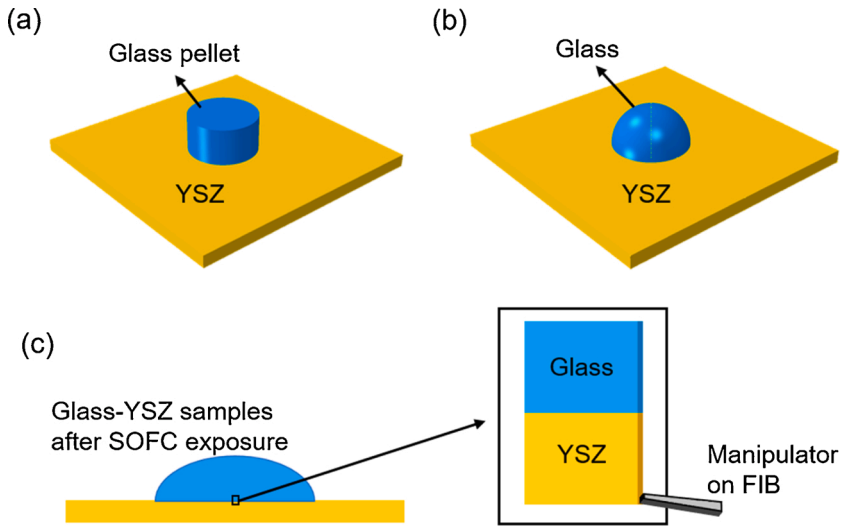

Fig. 1. Schematic of glass-YSZ substrate sample at the **(a)** pre-sintered, **(b)** post-sintered processes. **(c)** Cross-section view of post-exposure sample. The magnified image is inserted, showing the TEM samples including the glass/YSZ interface.

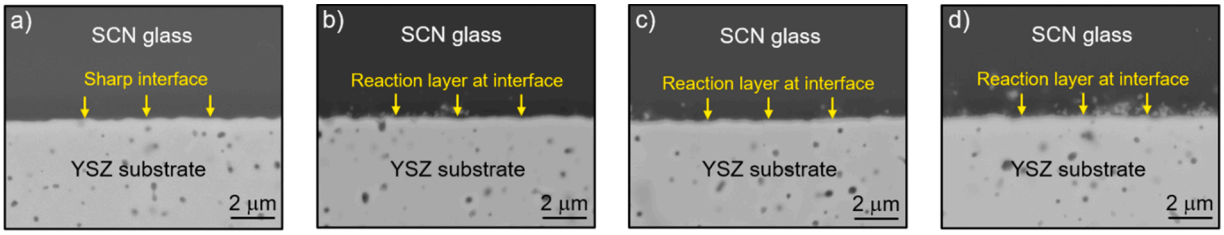

Fig. 2. Secondary electron SEM images showing SCN/YSZ interface of the samples exposed for **(a)** 100 h, **(b)** 10,000 h, **(c)** 25,000 h, and **(d)** 40,000 h at 800 °C in air.

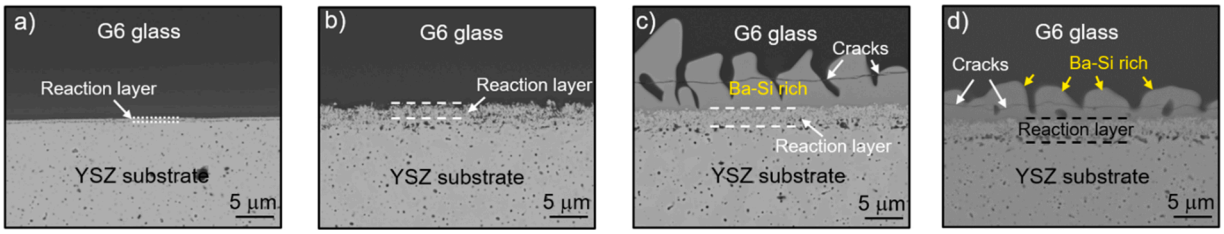

Fig. 3. Secondary electron SEM images showing G6/YSZ interface of the samples exposed for **(a)** 100 h, **(b)** 10,000 h, **(c)** 25,000 h, and **(d)** 40,000 h at 800 °C in air.

To further understand the characteristics of the glass-YSZ reaction layers, STEM was used for chemical and microstructural analysis. Fig. 5 shows a low-magnification high-angle annular dark field (HAADF) -STEM image and chemical analysis at the interfacial region of the SCN-YSZ system. The overview of the reaction layer after 40,000 h of exposure is shown via a HAADF-STEM image in Fig. 5a. Similar to the SEM image of Fig. 2d, the HAADF-STEM image confirms the presence of a thin reaction layer at the SCN/YSZ interface. Some Ca- and Ba-rich precipitates were also observed above this reaction layer in the SCN glass. EDS quantitative spectroscopy was performed in this region, and selected maps of representative elements are shown in Fig. 5b–e (EDS elemental maps of other major glass elements are shown in Fig. S2). As expected, zirconium (Zr) was found to be the primary element in the YSZ substrate (Fig. 5b), while Si is the main element in SCN glass (Fig. 5c). In the thin reaction layer at the interface, much higher concentrations of calcium (Ca) and Ba were found (Fig. 5d and e), with some amounts (~5 at.%–10 at.%) of Si not only within the reaction layer but also concentrated at the interface with the YSZ substrate (Fig. 5c). Additional quantitative analysis was performed with a 1-dimensional (1D) EDS line profile from point A to point B across the interface (Fig. 5a). The concentration of selected elements is shown in Fig. 5f, emphasizing the variation in the Si, Ca, and Ba concentration along the line. The curves clearly confirm the previous observation of Zr and Y present in the substrate and Si in the glass, whereas the reaction layer region was rich in Ca, Si, and Ba. An increase in Si concentration at the YSZ/thin reaction layer was also observed (Fig. 5c) which extends for ~50 nm into the thin layer, consistent with the 2D elemental map for Si. The concentrations of sodium (Na) and potassium (K) in the SCN glass near the interface were approximately 3 at. % (Fig. S2d), about 11 at.% less than their original concentrations. This phenomenon was due mainly to the consumption of these elements by the precipitation of crystalline phase from the glass (Na- and/or K-based crystalline phase formation) or the potential evaporation of certain species from the bulk glass during long-term exposure [14].

To identify the crystal structure of this thin reaction layer, an analysis of the region at the SCN-YSZ interface (marked in Fig. 5a) is show in Fig. 6. The HR STEM-HAADF image of the reaction layer is shown in Fig. 6a, along with its fast Fourier transform (FFT) (Fig. 6b). Darker

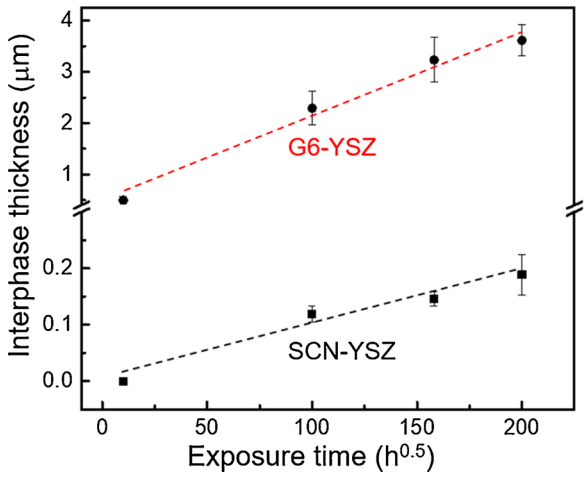

Fig. 4. Interphase thickness vs. square root of exposure time curves of **(a)** SCN-YSZ and **(b)** G6-YSZ samples.

atoms are surrounded by brighter ones, and the FFT shows both lattice diffractions and superlattice reflections. Based on previous EDS analysis, this thin reaction layer consists mainly of Ca, O, Si, and Ba, and the current analysis suggests that its structure (Fig. 6a) is similar to the standard CaO cubic structure (Fig. 6b and c) [20], except for the different contrast among atoms and the superlattice reflections. To identify the crystal structure of this reaction layer, more than 46 Ca (Ba)-Si-O published structures were analyzed and compared with the structure identified based on our STEM analysis in Table S1. Some of them matched the experimental structure but with errors greater than 7%. Density functional theory (DFT) and STEM electron energy loss spectroscopy (EELS) analysis were also used in an attempt to determine the crystal structure of the interfacial layer and are discussed in detail in the Supplementary section (Figs. S3 and S4).

A similar approach was applied to the characterization of the interfacial region of the G6-YSZ combination after 40,000 h of exposure. The low-magnification HAADF-STEM image in Fig. 7a outlines the morphology of the 3.3 μm thick reaction layer formed between the G6 glass (top) and the YSZ substrate (bottom) in the image. The reaction layer consisted of rod-shaped grains and some voids, with generate dark contrast of the region in the contact with the YSZ substrate. STEM-EDS quantified elemental maps (Fig. 7b–e) highlight that Zr and Y are distributed mainly in the YSZ substrate and within the reaction layer (Fig. 7b and d), whereas Si and Ba are present in the glass phase and fill the voids atop the YSZ substrate (Fig. 7c and e). In addition, the contrast variation in quantified Zr and Y maps suggests a higher Zr level (higher intensity contrast) and lower Y level (lower intensity) within the reaction layer (34.6–55.5 at.% for Zr, 0.6–3.4 at.% for Y) than in the substrate region (~49.5 at.% for Zr, ~7.5 at.% for Y), indicating the lower Y content with increasing distance from the YSZ substrate into the reaction layer. In addition to the Zr-rich rods formed in the reaction layer, Si and Ba were also observed (Fig. 7c and e) to diffuse from the glass through the space between rods in the reaction layer to the YSZ substrate surface. A 1D EDS line profile (marked in Fig. 7a) was performed from the YSZ substrate to the G6 glass, across the two pores (Fig. 7f). The variation in the concentration of Si, Ba, and Na along the distance can be clearly observed. In the YSZ substrate, Zr (~ 50 at. %) and Y (~8 at.%) are the two main constituents, whereas chemical analysis of the pores revealed the presence of Si, Ba, and Na. In the reaction layer, Zr is the primary element (~55 at.%), while the Y concentration decreases to 1–4 at. %. In the G6 glass, the concentrations of Si (~30 at.%) and Ba (~15 at.%) were higher, with a much lower Zr concentration (reduced from ~40 at. % to ~5 at.%) and negligible Y concentration. Concentrations of Na and

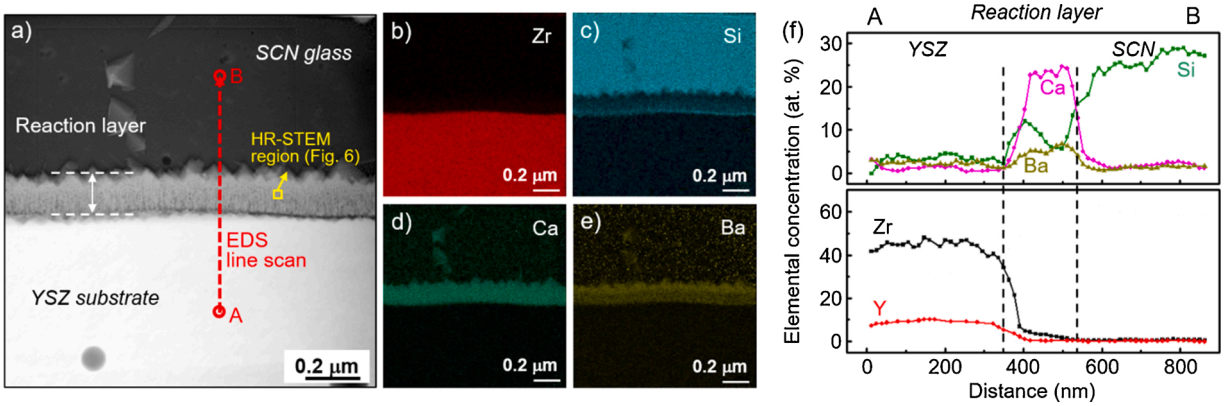

Fig. 5. **(a)** HAADF-STEM image of the interface of the SCN-YSZ sample exposed for 40,000 h in air with corresponding EDS elemental maps of **(b)** Zr, **(c)** Si, **(d)** Ca, and **(e)** Ba. **(f)** EDS line profiles showing concentration (at. %) of selected elements (Si, Ca, Ba, Zr, and Y) along the distance generated from the 1D line scan from A to B points marked in (5a).

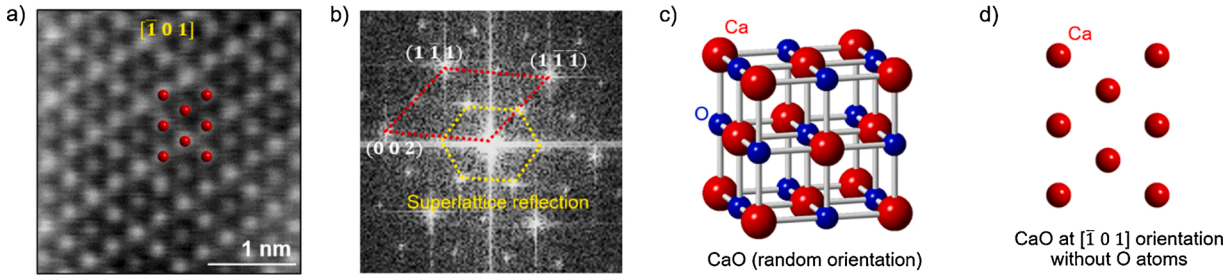

Fig. 6. **(a)** High-resolution HAADF-STEM image and **(b)** its FFT of the thin layer at the SCN/YSZ interface shows the Ca-Ba-Si-O phase at [$\bar{1}$ 0 1] orientation. **(c)** Standard CaO unit cell at random orientation with all atoms. **(d)** Standard CaO unit cell at [$\bar{1}$ 0 1] orientation without oxygen atoms.

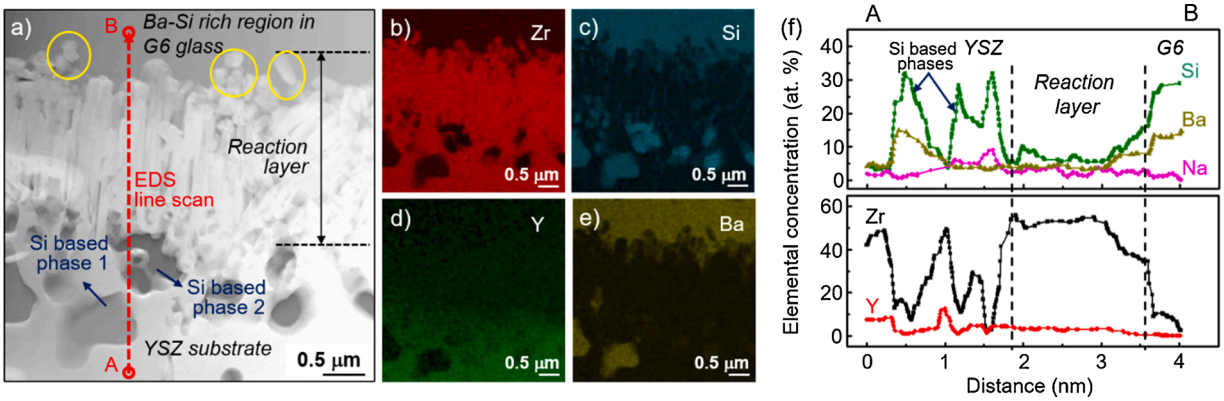

Fig. 7. **(a)** HAADF-STEM image at the interphase of the G6-YSZ sample exposed for 40,000 h in air with corresponding EDS elemental maps of **(b)** Zr, **(c)** Si, **(d)** Y, and **(e)** Ba. **(f)** EDS line profiles showing concentration (at. %) of selected elements (Si, Na, Ba, Zr, and Y) along the distance generated from the 1D line scan from A to B points marked in (8a).

K (not shown in Fig. 7f) remained relatively constant from the reaction layer to the G6 glass; they were less than 5 at.%. As expected, limitations of the EDS technique were found when attempting to measure the concentration of low-Z element like boron. Therefore, STEM-EELS analysis was conducted at the interfacial region, and a boron concentration was measured in the glassy Ba- and Si-rich region (Fig. S5).

To identify Zr-based phases, HR-STEM analysis was performed at both the reaction layer and at the YSZ substrate. These two specific regions are identified in the low-magnification image in Fig. 8a. The HR HAADF-STEM image of the reaction layer (Fig. 8b) shows a structure identified as monoclinic ZrO_2 oriented along the [010] zone axis. For comparison, the standard monoclinic ZrO_2 phase oriented along [010] obtained via HAADF-STEM is presented in Fig. 8c [21], which perfectly overlaps on the atomic image (Fig. 8b). For the YSZ substrate with higher Y concentration, the cubic ZrO_2 phase was confirmed by HR-STEM analysis oriented along the [010] direction (Fig. 8d). For comparison, standard cubic ZrO_2 unit cells oriented along the [010] direction are shown in Fig. 8e [22], which was fitted to the STEM image in Fig. 8d. The detailed crystalline information of ZrO_2 phases is summarized in Table 2.

The phase transformation of YSZ at the G6-YSZ interface was confirmed by Raman spectroscopy. Using principal component analysis, the maps of monoclinic, tetragonal, and cubic ZrO_2 at the G6-YSZ interface are shown in Fig. 9a–c, respectively. In each map, the

Table 2
Standard, STEM measured, and DFT calculated lattice constant and angles of the crystalline phases at SCN/YSZ interface and G6/YSZ interphase.

	Lattice constant (nm)			Angles (degree)		
	a	b	c	α	β	γ
CaO (standard, cubic) ref. [20]	0.483			90	90	90
Ca-Ba-Si-O layer (HR-STEM)	0.515	NA	0.526	88.28	91.72	NA
ZrO_2 (standard, monoclinic) ref. [29]	0.517	0.523	0.534	90	99.25	90
ZrO_2 (HR-STEM at interphase)	0.515	NA	0.517	NA	98.65	NA
ZrO_2 (standard, cubic) ref. [30]	0.514	0.514	0.514	90	90	90
ZrO_2 (HR-STEM at substrate)	0.525	NA	0.526	NA	90.21	NA

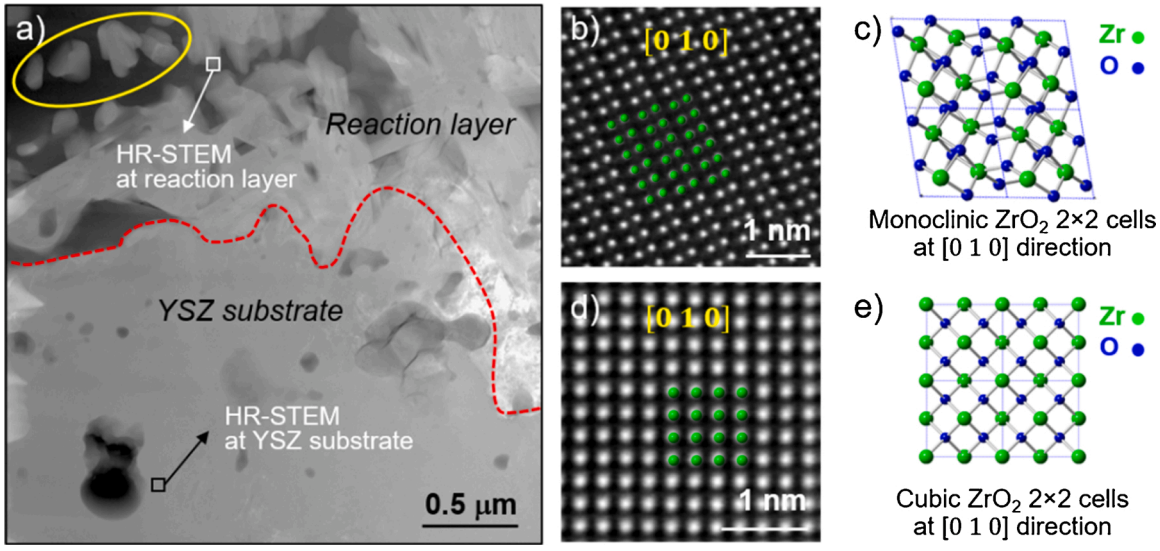

Fig. 8. **(a)** Low-magnification HAADF-STEM image of the YSZ substrate-interphase region. **(b)** High-resolution HAADF-STEM image of the interphase region showing the monoclinic ZrO_2 phase at [0 1 0] orientation. **(c)** Standard monoclinic ZrO_2 2 × 2 unit cells at [0 1 0] orientation with all the elements. **(d)** High-resolution HAADF-STEM image at YSZ substrate region shows the cubic ZrO_2 phase at [0 1 0] orientation. **(e)** Standard monoclinic ZrO_2 2 × 2 unit cells at [0 1 0] orientation with all the elements.

brighter contrast indicates a higher concentration of the corresponding phase. From these maps, we found that the monoclinic phase/layer is in direct contact with the glass, and it is much thicker than the tetragonal phase/layer (which is between the monoclinic layer and the cubic substrate). The YSZ substrate is entirely cubic, while a small portion of cubic phase is detected in the tetragonal and monoclinic layers, indicating the cubic phase is not fully transformed in the reaction region. The averaged Raman spectra of each phase (Fig. 9a–c) are shown in Fig. 9d, with their unique peaks marked by asterisks [23]. From the spectra, we also noted the weak residual tetragonal and cubic peaks in the monoclinic spectrum and the weak residual monoclinic and cubic peaks in the tetragonal spectrum that the principal component analysis was unable to completely separate. Some peaks identified in the spectra of monoclinic and tetragonal phases are not the ZrO_2 peaks but most likely are associated with the G6 glass, which diffused into the reaction region. Further Raman spectroscopy analysis supported STEM results from the sample exposed for 40,000 h, in which phase transformation of ZrO_2 from the YSZ substrate to reaction region was observed. Additional Raman spectroscopy analysis was also performed at the SCN-YSZ interface after 40,000 h exposure and there was no evidence of any phase transformation of the ZrO_2 phase (Fig. S6).

4. Discussion

In the multi-component silicate glasses investigated in this study, silica (SiO_2) acts as the network former [24] and determines the thermal and adhesion/wetting properties of the glasses [24]. G6 glass contained B_2O_3, (boron concentration ~15 at.%), which also acts as a network former and affects the thermal and wetting properties of the glass [25,26]. High concentrations of alkali metal oxides (Na_2O and K_2O) and alkaline earth oxides (MgO, CaO, and BaO) were also present in both glasses. These oxides are network modifiers and can affect the thermal and physical properties of the glasses. The major difference in the network modifiers between SCN and G6 is their overall concentrations (31.7 vs. 24.3 at. %). A higher concentration of modifiers induces a higher thermal expansion coefficient and lower glass-transition temperature of the glass [27] and then changes its devitrification resistance. Both glasses contain small amounts of Al_2O_3, which can work as either network former or modifier. It also hinders phase separation and changes the viscosity of the glasses [5]. Other oxides like TiO_2 in SCN and ZnO in G6 also regulate the thermal properties of the glasses [26].

Unlike two- or three-component glasses, the role of multiple components can be difficult to ascertain. For example, according to trends reported in previous studies, the devitrification resistance of SCN glasses should be enhanced more than that of G6 because of a higher concentrations of SiO_2 and network modifiers and a lower concentration of additives [5,24–27]. However, in the current work, devitrification occurred at the SCN/YSZ interface via the formation of a Ca-based thin reaction layer, but was absent at the G6/YSZ interface. A region rich in Ba and Si was formed by glass phase separation at the G6/YSZ interface (Figs. 3 and 7) with its short-range ordered structure maintained (Fig. S1). This result further confirmed a previous study in which bulk G6 glass exhibited higher resistance to devitrification at the temperatures and environments investigated [14].

The Ca-based thin reaction layer at the SCN/YSZ interface can significantly slow diffusion interactions between the glass and the YSZ substrate [28]. The Zr and Y concentrations in the substrate dramatically decreased from the substrate to the Ca-Ba-Si-O thin reaction layer (Fig. 5f). Similarly, the glass and thin reaction layer elements Si, Ca, and Ba—even though they had much higher concentrations in the glass or in the thin reaction region—decreased to less than 5 at. % once they reached the YSZ substrate. Despite these changes in the glass, even after 40,000 h exposure, the YSZ substrate at the interface maintained its cubic structure, as confirmed by Raman analysis in Fig. S6. Therefore, this Ca-Ba-Si-O reaction layer contributed to maintaining the stability of the YSZ substrate at the substrate-glass interface.

For the G6-YSZ system, instead of a thin reaction layer, a thicker reaction layer was formed between the G6 glass and the YSZ (Fig. 7). Furthermore, there was evidence of significant elemental diffusion in the vicinity of the glass/YSZ interface leading to the formation of an interdiffusion zone (Figs. 3 and 7). In this zone, Zr and Y diffused from the substrate and as well as glass elements Si, Ba, and Na (Fig. 7). Also, a phase change in Zr_2O was observed from the cubic Zr_2O phase (YSZ substrate) to a monoclinic structure found in the reaction layer (Fig. 8). Further Raman spectroscopy measurements confirmed the cubic-to-tetragonal-to-monoclinic phase transformation (Fig. 9). Such a phase transformation can be explained by diffusion processes in the reaction layer. With the addition of 8 mol % of Y_2O_3, the cubic phase of ZrO_2 can be stabilized at room temperature [29–31]. According to the STEM-EDS results (Fig. 7), more Y was detected in the YSZ substrate (~8 at. %) than in the reaction region (1–4 at. %), whereas the Zr concentration exhibited no obvious changes from the thick reaction layer/YSZ interface (~50 at.%) to ~2/3 of the thickness of the overall reaction layer (~50 at. %). Therefore, the YSZ substrate is expected to maintain the cubic phase (Figs. 8b and 9 c), whereas the reaction layer contains a low-temperature monoclinic Zr_2O phase (Figs. 8d and 9 a, b) resulting from the outward diffusion of Y [32]. Besides the continuous rod-shaped ZrO_2-based structure, some isolated ZrO_2 islands were also observed in the Ba-Si-rich region (circled in Figs. 7a and 8 a). The formation of these ZrO_2 islands was likely controlled by a dissolution-reprecipitation mechanism [32–34], which was reported by Stott et al. at the interfaces of silicate glass/YSZ thermal barrier coating systems, although at a much higher temperatures (1400–1500 °C) but much shorter times (20–120 hours) [35]. They also noted a lower concentration of Y in monoclinic ZrO_2 islands/precipitates [35], similar to that observed in the current work, which shows that a high-temperature reaction between silicate glass and YSZ can be achieved at lower temperatures with extended exposure time. The loss of Y from YSZ might affect the ionic conductivity at the ZrO_2-based interphase [36–38]. However, because the thickness of the reaction layer (several micrometers after 40,000 h of exposure) was negligible compared with the overall thickness of the ZrO_2 substrate (~0.8 mm), and because these reactions occur in a region of the cell where no electrochemical activity is expected, then these changes are not expected to affect the operation of SOFCs. However, the

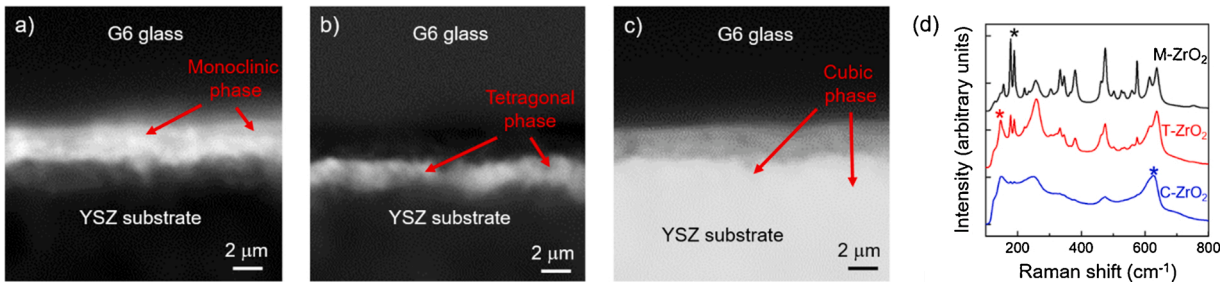

Fig. 9. Raman maps of ZrO_2 at G6/YSZ interface with **(a)** monoclinic, **(b)** tetragonal, and **(c)** cubic structure. **(d)** Average Raman spectra from monoclinic, tetragonal, and cubic maps in (a) to (c).

phase transformations experienced by YSZ could be accompanied by volumetric changes during heating/cooling cycles, which could affect the structural integrity of the interface.

For a quantitative understanding of the diffusion processes at the interface, the diffusion coefficients of selected elements were estimated from experimental data using Fick's second law [39]. The concentration, *c(x, t)*, of a diffusion element in one dimension evolves as a function of time *t* by,

$$\ln(c(x,t)) = -\frac{1}{4Dt}x^2 + b, \quad (1)$$

where *x* is the position of the diffused element in the diffusion dimension (cm), *D* is the diffusion coefficient ($cm^2\ s^{-1}$), and *b* is a constant. The *c(x, t)* and *x* values of selected elements across the interfaces of the 40,000 h samples were acquired from the EDS data shown in Figs. 5f and 8 f; and then the *ln(c(x, t))* vs. x^2 are plotted in Fig. 10. By linear regression, the values of the diffusion coefficient *D* were calculated from the slope of the *ln(c(x))* vs. x^2 curves. In the SCN-YSZ 40,000 h sample, the Ca-based reaction layer, which was generated at the early stage of high-temperature exposure, served as a "diffusion barrier" layer that hindered the diffusion of glass species into the YSZ substrate, and vice versa. Based on the slopes of the *ln(c(x, t))* vs. x^2 plots of these elements, their diffusion coefficients at 800 °C in air for up to 40,000 h were 2.2×10^{-19} $cm^2\ s^{-1}$ for Zr, 2.3×10^{-19} $cm^2\ s^{-1}$ for Y, and 3.3×10^{-19} $cm^2\ s^{-1}$ for Si. These values were relatively close to one another, indicating mass exchanges between YSZ substrate and SCN glass were very mild.

The behavior observed in the G6-YSZ system was different from that of SCN-YSZ. Interdiffusion occurred between elements from the YSZ substrate and the G6 glass at the interface during long-term exposure. As no "diffusion insulation" layer was observed between the substrate and the glass after high-temperature exposure, the diffusing elements formed a thicker interdiffusion region (reaction layer). The concentration- and position-related information, with related linear fits of selected elements Zr, Y, Si, and Ba in the interdiffusion (reaction layer) region, are summarized in Fig. 10b. Their diffusion coefficients were calculated based on Eq. (1), yielding values of 8.3×10^{-18} $cm^2\ s^{-1}$ for Zr (from YSZ to G6 glass), 1.5×10^{-18} $cm^2\ s^{-1}$ for Y (from YSZ to G6 glass), 5.2×10^{-18} $cm^2\ s^{-1}$ for Si (from G6 glass to YSZ), and 4.8×10^{-18} $cm^2\ s^{-1}$ for Ba (from G6 glass to YSZ). Based on the calculated diffusion coefficients, we note that Zr diffused five times faster than Y into the G6 glass. As a result, the Zr/Y ratio grew increasingly larger as these elements diffused deeper and deeper into the interdiffusion (reaction layer) region from the substrate, as was confirmed by chemical analysis at the G6-YSZ interface (Fig. 7). As discussed above, the decreasing Y concentration in YSZ led to phase transformations (Figs. 8 and 9).

It was found that the Si/Ba ratio in the interdiffusion layer formed at the interface between G6 glass and YSZ, was relatively constant. Si and Ba were also detected in pores in the YSZ substrate, indicating those two elements penetrated through the reaction layer and filled pores inside the substrate. In addition, in the reaction layer region, some Si and a few Ba atoms were concentrated at the boundaries of the rod-shaped monoclinic ZrO_2 grains. The segregation of these atoms at such a preferred site suggests the actual diffusion process at certain parts of the reaction layers occurred along grain boundaries rather than through the bulk [40,41].

Comparison of the diffusion coefficients of selected elements between SCN-YSZ and G6-YSZ indicated that the values of the SCN-YSZ system were much smaller than those for G6-YSZ. For example, the diffusion rates of the substrate elements (Zr and Y) were ~37 and 6 times faster, respectively, through the reaction layer of G6-YSZ sample than through the thinner Ca-Ba-Si-O reaction layer at the SCN-YSZ interface. A similar result was also found for Si. Therefore, the Ca-Ba-Si-O layer in the SCN-YSZ could reduce the substrate/glass interdiffusion rate during SOFC operation. As confirmed by previous and current studies, the formation of this thin diffusion barrier was due to the lower devitrification resistance of the SCN glass [14,15]. In the G6-YSZ system, the glass exhibited greater resistance to devitrification although the degree of interaction with YSZ was much greater. As reported in our previous work [15], the viscosity of SCN glass at 800 °C was about two times larger than that of G6 glass. Therefore, G6 will have an enhanced ability to infiltrate when in contact with YSZ at 800 °C, which will facilitate the diffusion process at the G6-YSZ interface.

5. Summary

In this study, two commercial multicomponent silicate glasses (SCN and G6) were sintered on a YSZ substrate. The thermal and chemical stabilities at the glass/YSZ substrate interface as a function of exposure time up to 40,000 h in air at 800 °C were investigated. With increasing exposure time, it was found that reaction layers had formed at the glass-substrate interface. A thin crystalline Ca-Ba-Si-O reaction layer was observed at the SCN-YSZ interface after exposure times of 10,000 h or longer. This layer grew slowly with time and served as a barrier for interactions between the glass and the substrate. A much thicker interdiffusion region was observed at the G6-YSZ interface, and a diffusion-induced cubic-to-tetragonal-to-monoclinic ZrO_2 transformation was

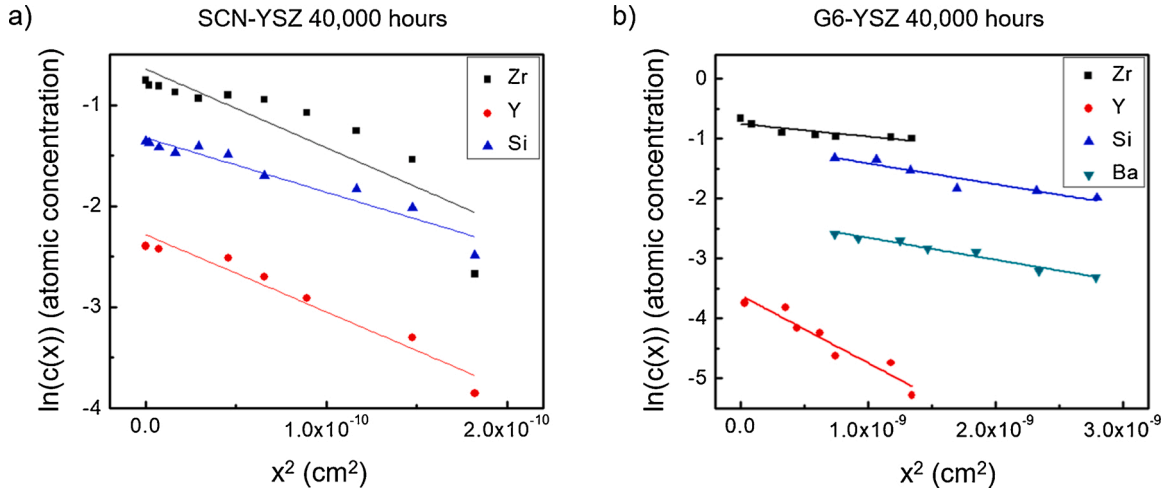

Fig. 10. The concentration vs. the position of the diffused element plots of (a) Zr, Y, and Si crossing the Ca-Ba-Si-O layer of the 40,000 h SCN-YSZ sample and (b) Zr, Y, Si, and Ba crossing the interdiffusion region of the 40,000 h G6-YSZ sample. Linear fitting was applied on each element, and their diffusion coefficients can be calculated from fitting lines.

observed in the YSZ substrate at the interface. From a sealing perspective, the greater stability of the interface between SCN and YSZ would be preferred, compared to that between G6 and YSZ. However, these findings need to be weighted in combination with other processes that take place in the bulk, such as the evolution of porosity and crystalline precipitation.

CRediT authorship contribution statement

Qianying Guo: Electron microscopy, formal analysis, writing first draft of manuscript. **Tianli Feng:** density functional theory calculations. **Sokrates T. Pantelides**: guiding density functional theory calculations. **Michael J. Lance**: Raman spectroscopy. **Kinga A. Unocic**: microscopy, characterization guidance, methodology for the paper, manuscript editing, guidance in figure selection and design, discussions on data analysis. **Edgar Lara-Curzio**: Project design, project direction, methodology, data analysis, and final manuscript editing.

All authors read and contributed to the revision of the manuscript.

Declaration of Competing Interest

The authors declare that they have no known competing financial interests or personal relationships that could have appeared to influence the work reported in this paper.

Acknowledgments

This work has been authored by UT-Battelle, LLC, under contract no. DE-AC05-00OR22725 with the US Department of Energy (DOE). This research work was sponsored by DOE, Office of Fossil Energy & Carbon Management, Solid Oxide Fuel Cells Core Technology Program at Oak Ridge National Laboratory (ORNL). The authors are grateful for the support of National Energy Technology Laboratory program managers Rin Burke and Shailesh Vora. Research was supported by the Center for Nanophase Materials Sciences (CNMS), which is sponsored by the Scientific User Facilities Division, Office of Basic Energy Sciences, DOE. The FEI Talos F200X STEM was used as part of the Nuclear Science User Facilities. We acknowledge ORNL's Fuel Cycle Materials Characterization Group for use of the Raman spectrometer. Theoretical work by T.L. F. and S.T.P. is supported in part by DOE grant DE-FG0209ER46554 and by the McMinn Endowment. Computations were performed at the National Energy Research Scientific Computing Center (NERSC), a DOE Office of Science, User Facility funded through contract no. DE-AC02-05CH11231. The authors thank their ORNL colleagues Beth Armstrong and David Mitchell for reviewing the manuscript and Beth Armstrong, Dana McClurg, Alexis Flores-Betancourt, Christina Padilla, Andres Marquez Rossy, Dorothy W. Coffey, and Tom. S. Geer for technical support. This manuscript has been authored by UT-Battelle, LLC, under contract DE-AC05-00OR22725 with the US Department of Energy (DOE). The US government retains and the publisher, by accepting the article for publication, acknowledges that the US government retains a nonexclusive, paid-up, irrevocable, worldwide license to publish or reproduce the published form of this manuscript, or allow others to do so, for US government purposes. DOE will provide public access to these results of federally sponsored research in accordance with the DOE Public Access Plan (http://energy.gov/downloads/doe-public-access-plan).

References

[1] N.Q. Minh, Solid oxide fuel cell technology—features and applications, Solid State Ion. 174 (1-4) (2004) 271–277.
[2] R.N. Singh, Sealing technology for solid oxide fuel cells (SOFC), Int. J. Appl. Ceram. Technol. 4 (2) (2007) 134–144.
[3] Y.-S. Chou, E.C. Thomsen, R.T. Williams, J.-P. Choi, N.L. Canfield, J.F. Bonnett, J. W. Stevenson, A. Shyam, E. Lara-Curzio, Compliant alkali silicate sealing glass for solid oxide fuel cell applications: thermal cycle stability and chemical compatibility, J. Power Sources 196 (5) (2011) 2709–2716.
[4] S.M. Haile, Fuel cell materials and components, Acta Mater. 51 (19) (2003) 5981–6000.
[5] M. Mahapatra, K. Lu, Glass-based seals for solid oxide fuel and electrolyzer cells–a review, Mater. Sci. Eng. R Rep. 67 (5-6) (2010) 65–85.
[6] S.-B. Sohn, S.-Y. Choi, G.-H. Kim, H.-S. Song, G.-D. Kim, Stable sealing glass for planar solid oxide fuel cell, J. Non. Solids 297 (2-3) (2002) 103–112.
[7] W. Fischer, J. Malzbender, G. Blass, R. Steinbrech, Residual stresses in planar solid oxide fuel cells, J. Power Sources 150 (2005) 73–77.
[8] W. Surdoval, E. Lara-Curzio, J. Stevenson, J.T. Muth, B.L. Armstrong, A. Shyam, R. M. Trejo, Y. Wang, Y.S. Chou, T.R. Shultz, Engineered glass seals for solid-oxide fuel cells, Google Patents, 2017.
[9] Y.-S. Chou, J.W. Stevenson, J.-P. Choi, Long-term evaluation of solid oxide fuel cell candidate materials in a 3-cell generic short stack fixture, Part II: sealing glass stability, microstructure and interfacial reactions, J. Power Sources 250 (2014) 166–173.
[10] S. Ghosh, P. Kundu, A.D. Sharma, R.N. Basu, H.S. Maiti, Microstructure and property evaluation of barium aluminosilicate glass-ceramic sealant for anode-supported solid oxide fuel cell, J. Eur. Ceram. Soc. 28 (1) (2008) 69–76.
[11] S.-E. Lin, Y.-R. Cheng, W. Wei, Synthesis and long-term test of borosilicate-based sealing glass for solid oxide fuel cells, J. Eur. Ceram. Soc. 31 (11) (2011) 1975–1985.
[12] S. Reis, R.K. Brow, Designing sealing glasses for solid oxide fuel cells, J. Mater. Eng. Perform. 15 (4) (2006) 410–413.
[13] S.J. Widgeon, E.L. Corral, M.N. Spilde, R.E. Loehman, Glass-to-metal seal interfacial analysis using electron probe microscopy for reliable solid oxide fuel cells, J. Am. Ceram. Soc. 92 (4) (2009) 781–786.
[14] A. Shyam, R. Trejo, D. McClurg, A. Ladouceur, M. Kirkham, X. Song, J. Howe, E. Lara-Curzio, Microstructural evolution in two alkali multicomponent silicate glasses as a result of long-term exposure to solid oxide fuel cell environments, J. Mater. Sci. 48 (17) (2013) 5880–5898.
[15] R. Trejo, E. Lara-Curzio, A. Shyam, M.J. Kirkham, V. Garcia-Negron, Y. Wang, Physical and mechanical properties of barium alkali silicate glasses for SOFC sealing applications, Int. J. Appl. Glass Sci. 3 (4) (2012) 369–379.
[16] M. Schaffer, B. Schaffer, Q. Ramasse, Sample preparation for atomic-resolution STEM at low voltages by FIB, Ultramicroscopy 114 (2012) 62–71.
[17] J. Mayer, L.A. Giannuzzi, T. Kamino, J. Michael, TEM sample preparation and FIB-induced damage, MRS Bull. 32 (5) (2007) 400–407.
[18] Y.-S. Chou, E.C. Thomsen, J.-P. Choi, J.W. Stevenson, Compliant alkali silicate sealing glass for solid oxide fuel cell applications: combined stability in isothermal aging and thermal cycling with YSZ coated ferritic stainless steels, J. Power Sources 197 (2012) 154–160.
[19] H. Aydin, C. Korte, M. Rohnke, J. Janek, Oxygen tracer diffusion along interfaces of strained Y_2O_3/YSZ multilayers, J. Chem. Soc. Faraday Trans. 15 (6) (2013) 1944–1955.
[20] W. Primak, H. Kaufman, R. Ward, X-ray diffraction studies of systems involved in the preparation of alkaline earth sulfide and selenide phosphors, J. Am. Chem. Soc. 70 (6) (1948) 2043–2046.
[21] Jt. McCullough, K. Trueblood, The crystal structure of baddeleyite (monoclinic ZrO2), Acta Crystallogr. 12 (7) (1959) 507–511.
[22] R. Ploc, The lattice parameter of cubic ZrO_2 formed on zirconium, J. Nucl. Mater. 99 (1) (1981) 124–128.
[23] M. Ishigame, T. Sakurai, Temperature dependence of the Raman spectra of ZrO_2, J. Am. Ceram. Soc. 60 (7-8) (1977) 367–369.
[24] C. Lara, M. Pascual, A. Duran, Glass-forming ability, sinterability and thermal properties in the systems RO–BaO–SiO_2 (R= Mg, Zn), J. Non. Solids 348 (2004) 149–155.
[25] K.S. Weil, The state-of-the-art in sealing technology for solid oxide fuel cells, JOM 58 (8) (2006) 37–44.
[26] V. Haanappel, V. Shemet, S. Gross, T. Koppitz, N. Menzler, M. Zahid, W. Quadakkers, Behaviour of various glass–ceramic sealants with ferritic steels under simulated SOFC stack conditions, J. Power Sources 150 (2005) 86–100.
[27] K.D. Meinhardt, D.-S. Kim, Y.-S. Chou, K.S. Weil, Synthesis and properties of a barium aluminosilicate solid oxide fuel cell glass–ceramic sealant, J. Power Sources 182 (1) (2008) 188–196.
[28] L. Rose, M. Menon, K. Kammer, O. Kesler, P.H. Larsen, Processing of Ce1-xGdxO_2-δ (GDC) thin films from precursors for application in solid oxide fuel cells, Adv. Mat. Res. (2007) 293–298.
[29] C. Pascual, P. Duran, Subsolidus phase equilibria and ordering in the system ZrO_2-Y_2O_3, J. Am. Ceram. Soc. 66 (1) (1983) 23–27.
[30] V. Lanteri, R. Chaim, A.H. Heuer, On the microstructures resulting from the diffusionless cubic→Tetragonal transformation in ZrO_2-Y_2O_3 alloys, J. Am. Ceram. Soc. 69 (10) (1986) C-258–C-261.
[31] H.-S. Yang, G.-R. Bai, L. Thompson, J. Eastman, Interfacial thermal resistance in nanocrystalline yttria-stabilized zirconia, Acta Mater. 50 (9) (2002) 2309–2317.
[32] J.M. Drexler, A.L. Ortiz, N.P. Padture, Composition effects of thermal barrier coating ceramics on their interaction with molten Ca–Mg–Al–silicate (CMAS) glass, Acta Mater. 60 (15) (2012) 5437–5447.
[33] J. Wu, H.-b. Guo, Y.-z. Gao, S.-k. Gong, Microstructure and thermo-physical properties of yttria stabilized zirconia coatings with CMAS deposits, J. Eur. Ceram. Soc. 31 (10) (2011) 1881–1888.
[34] R. Hellmann, S. Cotte, E. Cadel, S. Malladi, L.S. Karlsson, S. Lozano-Perez, M. Cabié, A. Seyeux, Nanometre-scale evidence for interfacial dissolution–reprecipitation control of silicate glass corrosion, Nat. Mater. 14 (3) (2015) 307–311.

[35] F. Stott, D. De Wet, R. Taylor, Degradation of thermal-barrier coatings at very high temperatures, MRS Bull. 19 (10) (1994) 46–49.
[36] A. Cheikh, A. Madani, A. Touati, H. Boussetta, C. Monty, Ionic conductivity of zirconia based ceramics from single crystals to nanostructured polycrystals, J. Eur. Ceram. Soc. 21 (10-11) (2001) 1837–1841.
[37] J. Luo, D.P. Almond, R. Stevens, Ionic mobilities and association energies from an analysis of electrical impedance of ZrO_2–Y_2O_3 alloys, J. Am. Ceram. Soc. 83 (7) (2000) 1703–1708.
[38] A. Lakki, R. Herzog, M. Weller, H. Schubert, C. Reetz, O. Görke, M. Kilo, G. Borchardt, Mechanical loss, creep, diffusion and ionic conductivity of ZrO_2-8 mol% Y_2O_3 polycrystals, J. Eur. Ceram. Soc. 20 (3) (2000) 285–296.
[39] M. Kilo, M.A. Taylor, C. Argirusis, G. Borchardt, B. Lesage, S. Weber, S. Scherrer, H. Scherrer, M. Schroeder, M. Martin, Cation self-diffusion of 44 Ca, 88 Y, and 96 Zr in single-crystalline calcia-and yttria-doped zirconia, J. Appl. Phys. 94 (12) (2003) 7547–7552.
[40] K. Malek, M.-O. Coppens, Effects of surface roughness on self-and transport diffusion in porous media in the Knudsen regime, Phys. Rev. Lett. 87 (12) (2001), 125505.
[41] R.A. De Souza, M. Martin, Probing diffusion kinetics with secondary ion mass spectrometry, MRS Bull. 34 (12) (2009) 907–914.